

A search for damped Lyman- α systems towards radio-loud quasars I: The optical survey.*

Sara L. Ellison¹, Brian A. York¹, Max Pettini², Nissim Kanekar³.

¹*Department of Physics and Astronomy, University of Victoria, Victoria, B.C., V8P 1A1, Canada*

²*Institute of Astronomy, Madingley Rd., Cambridge, CB3 0HA, UK*

³*National Radio Astronomy Observatory, 1003 Lopezville Road, Socorro, NM 87801, USA*

24 October 2018

ABSTRACT

We present the results from the optical component of a survey for damped Lyman- α systems (DLAs) towards radio-loud quasars. Our quasar sample is drawn from the Texas radio survey with the following primary selection criteria: $z_{\text{em}} \geq 2.4$, optical magnitudes $B \leq 22$ and 365 MHz flux density $S_{365} \geq 400$ mJy. We obtained spectra for a sample of 45 QSOs with the William Herschel Telescope, Very Large Telescope and Gemini-North, resulting in a survey redshift path $\Delta z = 38.79$. We detect nine DLAs and one sub-DLA, with a mean absorption redshift $\langle z \rangle = 2.44$. The DLA number density is $n(z) = 0.23^{+0.11}_{-0.07}$, in good agreement with the value derived for DLAs detected in the Sloan Digital Sky Survey at this redshift. The DLA number density of our sample is also in good agreement with *optically-complete* radio-selected samples, supporting previous claims that $n(z)$ is not significantly affected by dust obscuration bias. We present $N(\text{H I})$ column density determinations and metal line equivalent width measurements for all our DLAs. The low frequency flux density selection criterion used for the quasar sample implies that all absorbers will be suitable for follow-up absorption spectroscopy in the redshifted H I 21 cm line. A following paper (Kanekar et al.) will present H I 21 cm absorption studies of, and spin temperature determinations for, our DLA sample.

Key words: surveys, quasars: absorption lines, galaxies: high redshift

1 INTRODUCTION

Damped Lyman- α systems (DLAs) currently provide the most complete means to study the gas-phase interstellar medium (ISM) of high redshift galaxies. Many hundreds of DLAs have now been identified (e.g. Prochaska, Herbert-Fort & Wolfe 2005), with chemical abundances derived for ~ 150 from high resolution optical spectroscopy (Prochaska et al. 2007). Such spectroscopy also permits studies of the gas velocity fields, although the interpretation can be complicated (Prochaska & Wolfe 1997; Haehnelt, Steinmetz & Rauch 1998; Maller et al. 2001). Few other physical quantities can be derived for DLAs in a wholesale manner. Although a handful of DLAs have been subjected to detailed

modelling of the ionization state of the ISM (e.g. Prochaska et al. 2002; Lopez et al. 2002; Tripp et al. 2005), have galactic counterparts identified (Møller et al. 2004 and references therein) or have size estimates (Lopez et al. 2005, but see Ellison et al. 2007), there are relatively few tools at our disposal to determine the physical characteristics of high redshift DLA galaxies. One example of a technique that relies on well-understood physics and has been widely applied to the Milky Way and Magellanic Clouds (e.g. Tumlinson et al. 2002), but is only recently realising its potential at high redshift, is the study of molecular hydrogen (Ge & Bechtold 1997; Ge, Bechtold & Kulkarni 2001; Ledoux et al. 2003; Sri-anand et al 2005). For example, in two DLAs which exhibit molecular H₂ absorption spanning a number of rotational levels, Noterdaeme et al. (2007a,b) have been able to compute the properties of the radiation fields as well as gas phase temperatures and densities. Another technique that can be used to probe the properties of absorption systems has been developed by Wolfe, Prochaska & Gawiser (2003) who use detections of \mathbb{Z} s (absorption from the excited fine-structure level of the ground state) to infer the star formation rate

* Based on observations made with (1) ESO Telescopes at the Paranal Observatories under programme IDs 075.A-0015(B) and 077.A-0139(A,B), (2) the Gemini-North Observatory under programme IDs GN-2005B-Q-60 and GN-2006A-Q-42 and (3) the William Herschel Telescope under programme IDs W/06A/P3 and W/06B/P5.

(SFR) in DLA galaxies. The downsides of these techniques are that they are both model-dependent and rely on the detection of uncommon species, so that they may present a somewhat biased view of the high redshift ISM. For example, the molecular hydrogen fraction is greater than $10^{-4.5}$ in only 4% of DLAs and sub-DLAs ($19 < \log N(\text{H I}) < 20.3$) when the metallicity is less than 1/20 of the solar value. This percentage rises to 35% for absorbers whose metallicity is greater than 1/20 of the solar value, indicating that molecule formation/survival is more successful in metal-rich, dustier systems (Noterdaeme et al. 2008). Zs is detected in about 60% of DLAs (Wolfe et al. 2008). It has also been shown by Wolfe et al. that the distribution of cooling rates (which is directly determined from the column densities of H I and Zs) is bimodal. These authors argue that this bimodality is due to an underlying difference in the mode of star formation, analogous to the bimodality that leads to the blue and red sequences in galaxies at low redshift. The strength of (and therefore ability to detect) Zs absorption [for a given $N(\text{H I})$] therefore depends on the properties of the galaxy.

H I 21 cm absorption studies of DLAs towards radio-loud quasars provide an alternative probe of the state of the ISM in high redshift galaxies (see Kanekar & Briggs 2004 for a review), through measurements of the H I spin temperature. The latter quantity is determined by combining measurements of the H I column density (determined, in DLAs, from the Lyman- α absorption line) and the H I 21 cm optical depth. In typical Galactic clouds, the spin temperature, T_s , of cold H I clouds (where collisions are sufficiently frequent to thermalise the H I 21 cm transition) is approximately the same as the gas kinetic temperature (e.g. Kulkarni & Heiles 1988); conversely, T_s is expected to be lower than the kinetic temperature for the warm phase of H I (e.g. Liszt 2001). For multi-phase lines of sight, the measured spin temperature can be shown to be the column-density-weighted harmonic mean of the spin temperatures of different phases (and is thus biased towards the phase with the lowest temperature). For example, a sightline with 10% of its gas at 100 K and 90% of its gas at 8000 K (typical temperatures of the cold and warm neutral media, CNM and WNM respectively) would have a measured spin temperature $T_s \sim 900$ K. H I 21 cm absorption studies of DLAs towards compact quasars thus provide information on the *distribution of gas in different temperature phases* and can be used to study the evolution of this temperature distribution with redshift (e.g. Wolfe & Davis 1979; Wolfe, Briggs & Jauncey 1981; de Bruyn et al. 1996; Carilli et al. 1996; Lane et al. 1998; Chengalur & Kanekar 2000; Kanekar & Chengalur 2001; Kanekar & Chengalur 2003).

DLA spin temperatures may also yield other clues to the character of high redshift galaxies, beyond the direct probe of the gas temperature. For example, there is evidence that T_s is connected with galaxy size and morphology (e.g. Chengalur & Kanekar 2000). In the local universe, large disk galaxies like the Milky Way and M31 tend to have significant cold gas fractions, yielding low harmonic mean spin temperatures, $T_s \lesssim 300$ K (Braun & Walterbos 1992; Braun 1997). Conversely, dwarf galaxies appear to have far larger fractions of the warm phase of H I with $T_s \gtrsim 1000$ K (e.g. Young & Lo 1997). Kanekar & Chengalur (2003) have argued that a similar connection between T_s and morphology

exists in DLAs, at least out to $z \sim 0.7$. If this relationship persists to higher redshifts, the spin temperature would be an excellent probe of galaxy morphology at redshifts where direct imaging of galaxies is extremely difficult. There is also tentative evidence for an anti-correlation between metallicity and spin temperature (Kanekar & Briggs 2004; Kanekar et al. in preparation), further suggesting that the gas temperature distribution in a typical DLA may be determined by global factors like mass, SFR, metallicity, etc. Finally, understanding whether the ISM of typical DLAs is dominated by the CNM or WNM has significant implications for modelling SFRs at high z (e.g. Wolfe et al. 2003).

Although the measurement of DLA spin temperatures holds great promise as a probe of the ISM in high z galaxies, there are a number of problems that need to be addressed. For example, although the C II* model of Wolfe et al. (2003) requires about half of the high z DLA population to have sizeable fractions of cold H I, this is apparently contradicted by the high spin temperatures universally measured in $z > 2$ DLAs prior to our survey (e.g. Carilli et al. 1996; Kanekar & Chengalur 2003; Kanekar et al. 2006, 2007). Only at $z < 1$ have spin temperatures $T_s \lesssim 300$ K been obtained (see Table 3 of Kanekar & Chengalur 2003). The reason behind the apparent dearth of low spin temperatures at high redshift has been the cause of considerable debate. One possibility is that the galaxy population at $z > 2$ is dominated by dwarfs, whereas at low redshift, a more diverse mix of morphologies exists (e.g. Kanekar & Chengalur 2001). Alternatively, it has been suggested that the high spin temperatures seen in high- z DLAs arise as an artefact of either low covering factors (e.g. Curran et al. 2005; Curran & Webb 2006) or differences between the optical and radio lines of sight (Wolfe et al. 2003).

One of the problems in untangling the issues described above is the small number of H I 21 cm absorption studies at $z > 2$. After nearly thirty years of searches prior to the present survey, there have been only five detections of H I 21 cm absorption in $z \gtrsim 1.8$ DLAs (Wolfe & Davis 1979; Wolfe et al. 1981; Wolfe et al. 1985; Briggs, Brinks & Wolfe 1997; Kanekar et al. 2006, 2007), with ~ 12 non-detections of absorption, yielding strong lower limits ($\gtrsim 1000$ K) on the spin temperature (e.g. Kanekar & Chengalur 2003). Most of these results have been obtained in the last decade, as the result of improved frequency coverage on telescopes like the Giant Metrewave Radio Telescope (GMRT) and the Green Bank Telescope (GBT).

The primary reason for the lack of spin temperature measurements in high- z DLAs is simply the paucity of known DLAs towards radio-loud QSOs. For example, only two of the ~ 500 DLAs detected in the SDSS-DR3 sample of Prochaska et al. (2005) lie towards QSOs with sufficient low-frequency flux density for follow-up 21 cm absorption studies. In addition, only two DLA surveys have specifically targeted radio-loud quasars, the Complete Optical and Radio Absorption Line System (CORALS) survey by Ellison et al. (2001) and the UCSD survey of Jorgenson et al. (2006). However, both of these surveys selected quasars on the basis of their high-frequency (2.7 – 5 GHz) flux density. Unfortunately, in many cases, the DLA detections occurred towards quasars whose flux density at low frequencies (corresponding to the redshifted H I 21 cm line) is insufficient for absorption follow-up. A significant improvement of T_s statistics clearly

requires a dedicated survey for DLAs towards quasars selected at frequencies of 300 – 500 MHz.

We have conducted precisely such an optical survey, specifically designed to detect DLAs towards radio-loud quasars selected at low frequencies. In theory (i.e. excluding issues related to local radio frequency interference), it should be possible to follow up every DLA detected in this survey with a search for redshifted H I 21 cm absorption. In this paper, we describe the optical portion of the survey, including the survey design and sample selection (section 2), observations and data reduction (sections 3 and 4) and the DLA detections, fits and statistical properties (section 5). The survey has already yielded the first detection of a low spin temperature DLA at $z \gtrsim 2$ (York et al. 2007). A following paper (Kanevar et al., in preparation) will present the H I 21 cm observations and inferred spin temperatures for the full sample of DLAs detected in the survey.

2 SAMPLE SELECTION

Our goal is to identify DLAs from optical, ground-based spectra towards radio-loud quasars that will be suitable for follow-up spectroscopy in the redshifted H I 21 cm line. In order to proceed efficiently with this search, we must therefore first identify a sample of quasars that is well characterised at both optical and radio wavelengths. The quasars must obviously be radio-loud, but we must specifically be careful to select targets that have sufficient flux at $1420/(1+z_{\text{abs}}) \sim 300 - 500$ MHz to permit later searches for redshifted H I 21 cm absorption. We selected the Texas radio survey (Douglas et al. 1996) as the most suitable for our purpose, due to its low frequency and wide area sky coverage. In brief, the Texas (TXS) survey was conducted with the Texas interferometer at 365 MHz between 1974 and 1983 and contains almost 67,000 discrete sources with arcsecond positional precision. The survey covers declinations between -35.5 degrees to $+71.5$ degrees and is complete to 0.4 Jy and 80% complete to 0.25 Jy (Douglas et al. 1996).

In order to select a sample of high redshift quasars from within the TXS survey, we used the NASA Extragalactic Database (NED) with the following search criteria:

- TXS sources classified as QSOs
- Redshifts $z_{\text{em}} \geq 2.40$
- 365 MHz flux density $S_{365} \geq 400$ mJy

This search yielded a total of 123 targets. From within this list, we excluded objects that we considered too faint at optical wavelengths for efficient follow-up (typically $B > 22$) and any targets which had already been included in previous DLA searches¹. In order to fill the ranges in right ascension suitable for scheduled observing runs, we relaxed these criteria in a few cases to include additional objects.

Observing time for this project was allocated at Gemini-North, the William Herschel Telescope (WHT) and the Very Large Telescope (VLT) in observing semesters from early 2005 until late 2006. The total telescope time allocated to this project amounted to 17.2 hours at the VLT, 32.2 hours

Table 1. Telescope time allocations

Telescope	Semester	Allocation	Actual
WHT	2005A	3 nights	3 nights
WHT	2006B	2 nights	1.5 nights
Gemini-North	2005B	19 hours	19 hours
Gemini-North	2006A	13.2 hours	9 hours
VLT	P75	2.2 hours	2.2 hours
VLT	P77	15 hours	15 hours

on Gemini-North (of which 28 were completed) and 5 nights at the WHT (see the next section and Table 1). Targets with B -band magnitudes brighter than 20.0 and declinations $\delta > -10$ were typically observed with the WHT. Fainter targets at northerly declinations were assigned to Gemini, whilst all targets with $\delta < -10$ were observed with the VLT. With these allocations, we were able to complete observations of 45 QSOs for our DLA search. The final list of quasars in our survey is given in Table 2.

3 OBSERVATIONS

Observing procedures differed from telescope to telescope. At both Gemini-North and the VLT, observations were carried out in queue/service mode, according to the practices (e.g. scheduling and calibration plans) of those particular observatories. The WHT observations were carried out in classic/visitor mode. We briefly describe the instrument configurations, run conditions and notable observing strategies for each telescope.

3.1 WHT observations

The Intermediate dispersion Spectrograph and Imaging System (ISIS) was used for our WHT observations. ISIS is a dual arm spectrograph whose red and blue channels can be fed through a selection of dichroics. Our observations only made use of the blue arm, since the entire Lyman- α forest could be covered with a single setting for our targets. We used the R300B grating which is blazed at 4000 Å and yields a total wavelength coverage of 3539 Å. However, there is significant vignetting with the 4096×2048 13 μm EEV CCD detector, such that the total unvignetted spectral coverage is approximately 2800 Å per tilt. The central wavelength for all targets observed with ISIS was 4600 Å, yielding a total unvignetted wavelength coverage of 3200 – 6000 Å, although in practice a high fraction of the flux is recovered out to 6200 Å. In some cases, a reasonable signal was also recovered slightly blueward of 3200 Å. Table 3 summarises the relevant instrument setup information.

The WHT observations were conducted during two runs: 3 nights in April 2005 and 2 nights in November 2006. The April run experienced mixed conditions, with some high cirrus, high humidity and seeing of 1.0 – 1.2 arcsec at the start of the run, improving to 0.5 arcsec and clear skies by

¹ 8 of the QSOs in our survey have subsequently also appeared in the DLA survey of Jorgenson et al. (2006).

Table 2. QSO observation log for optical observations

QSO	z_{em}	B mag	365 MHz flux density (Jy)	Telescope	Obs. date	Exposure time (s)	S/N pix^{-1}
TXS0017-307	2.67	20.0	0.496 ± 0.051	VLT	2006 Jul. 27	1000	8-80
TXS0211+296	2.87	20.5	0.412 ± 0.021	Gemini	2005 Nov. 1,2	7200	7-100
TXS0214-011	2.45	20.0	0.562 ± 0.045	WHT	2006 Nov. 23,24	7200	5-13
TXS0222+185	2.69	20.1	0.425 ± 0.041	WHT	2006 Nov. 24	7200	4-12
TXS0223+341	2.91	22.0	3.799 ± 0.034	Gemini	2006 Jul. 4,26,27	10800	6-40
TXS0229+230	3.42	22.0	0.581 ± 0.033	Gemini	2006 Jul. 28	10800	6-60
TXS0258+058	2.31	20.8	0.608 ± 0.028	WHT	2006 Nov. 24	3600	8-15
TXS0304-316	2.54	18.9	0.718 ± 0.058	VLT	2006 Aug. 16	1000	7-65
TXS0311+430	2.87	21.5	5.483 ± 0.052	Gemini	2005 Oct. 30, Nov. 2,3	14400	8-20
TXS0351+187	2.71	20.0	0.826 ± 0.021	WHT	2006 Nov. 24	7200	8-20
TXS0441+106	2.40	19.6	0.856 ± 0.027	WHT	2006 Nov. 24	5400	8-22
TXS0609+607	2.70	20.0	1.562 ± 0.033	WHT	2006 Nov. 24	7200	6-18
TXS0620+389	3.46	20.0	2.233 ± 0.081	WHT	2006 Nov. 24	7200	7-16
TXS0723+488	2.46	20.2	0.646 ± 0.019	Gemini	2005 Nov. 2,3	3600	6-60
TXS0859+433	2.41	20.7	0.606 ± 0.052	Gemini	2005 Nov. 4	7200	7-110
TXS0902+490	2.69	18.0	0.976 ± 0.024	WHT	2005 Apr. 17	1800	10-40
TXS0907+258	2.74	18.2	0.453 ± 0.032	WHT	2005 Apr. 16,18	1800	9-50
TXS0930+493	2.58	18.8	0.488 ± 0.021	WHT	2005 Apr. 18	3600	6-25
TXS0935+397	2.49	20.2	0.445 ± 0.039	Gemini	2005 Nov. 29	3600	7-50
TXS1013+524	2.45	19.9	0.846 ± 0.038	WHT	2005 Apr. 18	3600	4-13
TXS1017+109	3.15	18.7	1.642 ± 0.034	WHT	2005 Apr. 16,17	3600	17-30
TXS1025-264	2.66	18.4	1.735 ± 0.128	VLT	2006 Apr. 5	1000	25-75
TXS1048+347	2.52	20.4	0.574 ± 0.022	Gemini	2005 Dec. 4,22,24	7200	13-50
TXS1053+704	2.49	19.3	0.447 ± 0.023	WHT	2005 Apr. 17	5400	5-20
TXS1214+348	2.64	19.4	0.578 ± 0.052	WHT	2005 Apr. 18	3600	12-40
TXS1214+588	2.54	19.6	0.710 ± 0.058	WHT	2005 Apr. 18	3600	14-35
TXS1239+376	3.81	20.0	0.469 ± 0.019	WHT	2005 Apr. 17,18	7200	5-53
TXS1313+200	2.47	18.0	0.844 ± 0.025	WHT	2005 Apr. 19	3600	10-30
TXS1358+046	2.55	21.3	0.771 ± 0.027	VLT	2006 Apr. 3	4000	10-75
TXS1427+263	2.91	18.3	0.798 ± 0.029	WHT	2005 Apr. 17	2700	10-40
TXS1442+101	3.52	19.0	2.490 ± 0.210	WHT	2005 Apr. 18	3600	20-66
TXS1445-161	2.41	19.9	2.494 ± 0.053	VLT	2006 Apr. 3	1000	10-62
TXS1452+502	2.84	19.7	3.439 ± 0.146	WHT	2005 Apr. 17,18	4800	28-45
TXS1455+348	2.73	19.8	0.739 ± 0.051	WHT	2005 Apr. 19	5400	6-15
TXS1539+477	2.80	18.2	0.645 ± 0.018	WHT	2005 Apr. 17	3600	5-37
TXS1557+032	3.89	21.5	0.543 ± 0.070	VLT	2005 Apr. 10	4000	6-46
TXS1701+379	2.45	20.0	0.537 ± 0.053	WHT	2005 Apr. 19	5400	11-45
TXS1722+526	2.51	18.0	0.797 ± 0.021	WHT	2005 Apr. 18	2200	15-70
TXS2015+657	2.84	21.0	0.884 ± 0.062	Gemini	2006 May 23,27	5400	9-140
TXS2039+187	3.05	21.5	1.865 ± 0.027	VLT	2006 May 25,28	4000	7-140
TXS2127+348	2.40	19.5	0.515 ± 0.037	WHT	2006 Nov. 24	5400	15-30
TXS2131-045	4.34	21.5	0.622 ± 0.058	VLT	2006 May. 25	4000	16-35
TXS2211-251	2.50	20.1	2.829 ± 0.132	VLT	2006 May 28, Jun. 21	1000	8-65
TXS2320-312	2.54	18.8	1.592 ± 0.051	VLT	2006 May 15	1000	8-106
TXS2338+042	2.59	19.9	6.067 ± 0.147	WHT	2006 Nov. 23	7200	2-17

Table 3. Instrument set-ups

Telescope	Run dates	Instrument	Grating or grism	Slit width (arcsec)	CCD binning	Resolution FWHM (\AA)	Wavelength coverage (\AA)
WHT	2005 Apr. 16-18	ISIS Blue Arm	R300B	0.7-1.0	1x1	2.5	3200-6200
WHT	2006 Nov. 23-24	ISIS Blue Arm	R300B	1.0	1x1	2.5	3200-6200
Gemini-North	2005B	GMOS-N	B600	1.0	2x2	4.6	3700-6000
Gemini-North	2006A	GMOS-N	B600	1.0	2x2	4.6	3700-6000
VLT	Period 75	FORS2	600B	1.0	2x2	4.7	3500-6300
VLT	Period 77	FORS2	600B	1.0	2x2	4.7	3500-6300

the end of the third night. The slit width was chosen to track the conditions and varied from 1.0 to 0.7 arcsec. The November run experienced poorer conditions: seeing was 0.9 – 1.0 arcsec throughout, so the slit width was fixed at 1.0 arcsec. The second night of this run suffered from high humidity and the latter half was lost for this reason. Previous experience with ISIS revealed that the drift in wavelength calibration through the night can be significant, up to ~ 2 Å. We therefore took exposures for wavelength calibration (with the internal CuAr and CuNe lamps) after each target slew. We repeated the arc observations after every two on-target exposures of typically 1800 seconds each.

3.2 Gemini-North observations

We utilized the Gemini Multi-Object Spectrograph (GMOS) on Gemini-North. We used the B600 grating which is blazed at 4610 Å and yields a total (theoretical) wavelength coverage of 2760 Å per tilt. Our central wavelength was set to 4590 Å, with 30 Å offsets between exposures of a given target in order to cover the gaps between the 3 CCDs. Despite the theoretical coverage at the blue end of the spectral range, the very low efficiency of the telescope and instrument at these wavelengths meant that there was essentially zero flux blueward of 3700 Å. The effective wavelength coverage of our spectra suitable for a DLA search was therefore typically 3700 – 6000 Å. Table 3 summarises the relevant instrument setup information.

Observations were obtained during semesters 2005B and 2006A in queue mode. The observing conditions were set to be conducted in seeing conditions in the 85th percentile (1.0 arcsec or better) and with cloud coverage in the 70th percentile (0.3 magnitudes of extinction or less) with a fractional lunar illumination (FLI) less than 50%. A 1.0 arcsec slit was used throughout, which, combined with 2×2 on-chip binning, resulted in a FWHM resolution of approximately 4.6 Å. Exposures for wavelength calibration were obtained with a CuAr lamp, with one exposure taken at each central wavelength setting for each set of exposures. In practice, the observing sequence executed the science exposures centred at 4590 Å, followed by a wavelength calibration at that wavelength. The new grating tilt was then applied, a wavelength calibration taken at the central wavelength of 4620 Å, and then the science exposures at this wavelength.

3.3 VLT observations

We used the FOcal Reducer and low dispersion Spectrograph 2 (FORS2) at the VLT (UT1) with the 600B grism. The central wavelength of FORS2 is set by the combination of the grism and slit. With the slit width selected to be 1.0 arcsec, the total spectral coverage was 3500 – 6300 Å and FWHM resolution 4.7 Å (after 2×2 on-chip binning). Table 3 summarises the relevant instrument setup information.

A total of 17.2 hours on the VLT was distributed between Periods 75 and 76 (see Table 1). All observations were carried out in service mode. Observing conditions were set according to the target’s optical magnitude. Typically, the airmass was less than 1.5, the seeing better than 1.0 arcsec and FLI < 50%.

All calibration frames were obtained on the morning

following the science observations. The flats were obtained using an internal lamp and wavelength calibrations with a HgCd lamp. Extensive study of the stability of FORS2 indicates that there is no significant wavelength drift over this timescale.

4 DATA REDUCTION

The data obtained at the WHT and the VLT were reduced using tasks within the IRAF package. A master bias was constructed from typically 5 – 10 individual frames that were averaged together with a high pixel and cosmic ray rejection algorithm within the IRAF task *zerocombine*.

Flat fields at both the WHT and VLT were obtained from internal calibration lamps. In both cases, typically 5 exposures were taken. Each frame was visually inspected for potential saturation. Acceptable frames were averaged together with a cosmic ray rejection algorithm within the IRAF task *flatcombine*. The flats were normalized to remove any intrinsic spectral shape and the strong vignetting at the ends of the ISIS frames. There was no evidence for other strong detector- or instrument-induced effects, such as fringing.

All of the science frames were processed through the IRAF task *ccdproc* in order to fit and trim the CCD overscan, subtract the master bias and divide through by the master flat.

Cosmic rays were removed from the 2D frames with a custom written software (based on IRAF routines) for longslit spectra. First, the task *background* is used to fit the columns (spatial axis) of the 2D science (QSO) images. This fit is subtracted from the original 2D frame, effectively removing the sky². A median filter is then applied along the spectral axis, which removes the QSO signal. The resulting 2D frame has now been cleaned of both sky and QSO, leaving behind a cosmic ray image. A cosmic ray mask is then constructed by setting all cosmic ray pixels to have a value of 10000 and all other pixels to zero (in practice, this procedure is achieved in multiple steps, to identify both the cosmic ray ‘core’ and wings). The IRAF task *fixpix* is used to apply the mask to the science images.

The QSO spectra were extracted from the 2D images using the task *apall* with optimal extraction. The 1D spectra were wavelength calibrated by applying a polynomial solution derived from arc exposures obtained either during the night (WHT) or as part of the VLT daytime calibration plan. The arcs were processed through the *identify* task in IRAF, with the final wavelength solution applied using *dispcor*. A polynomial fit was applied to derive the final wavelength solution; a third – fifth order Legendre polynomial was usually required, which yielded typical RMS values < 0.1 Å. As noted in the previous section, there can be significant drift in the wavelength calibration of the ISIS instrument during the night. We therefore observed each target with the following sequence: arc, science exposure 1, science exposure 2, arc. During the calibration process, the arc taken immediately

² This simple procedure only works well in the absence of significant curvature. Since we are dealing with point sources, and instruments whose curvature is negligible over at least ± 200 pixels either side of the QSO, this technique works well.

adjacent to the science exposure was given a 2/3 weighting; the remaining arc was given a 1/3 weighting.

The GMOS reductions were executed using the Gemini IRAF package. This software operates within the IRAF infrastructure, but has been specifically designed to process data from Gemini instruments. All frames are run through the task *gprepare*, adding appropriate header information. The master bias frame was provided directly by Gemini science operations. Five flat field frames were obtained from observations of an internal calibration lamp. All were inspected for signs of saturation before constructing a master flat using the task *gsflat*. The flats were averaged together and a cosmic ray rejection algorithm used before the master flat was normalised. No significant fringing was present, due to the relatively blue wavelength coverage of our spectra. After this initial processing, the data were copied out of the Gemini multi-extension fits format, so that the remainder of the data reduction could be executed with standard IRAF tasks.

The rest of the GMOS data reduction proceeded as per the WHT and VLT processing. The 1D QSO spectra were extracted using optimal weighting in *apall*. A trace of the QSO position on the CCD was used to extract 1D arc spectra, which were obtained as observations interleaved with science exposures. Wavelength calibration was done using *identify* and *dispcor*. As for the WHT and VLT spectra, a third – fifth order Legendre polynomial was usually required to derive the wavelength solution, yielding typical RMS values $<0.1 \text{ \AA}$.

The wavelength calibrated 1D spectra were median combined using *scombine* with equal weightings. No flux calibration was attempted. The spectra of all of the QSOs observed in this survey are shown in Figure 1.

4.1 Notes on individual objects

TXS0351+187 is a broad absorption line (BAL) quasar. The broad feature at $\lambda_{\text{obs}} = 3750 \text{ \AA}$ that resembles a DLA is $\text{Ly}\beta$ associated with the BAL outflow.

TXS1013+235 is a BAL quasar.

TXS2034+046 is reported in Dodonov et al. (1999) to have an emission redshift $z_{\text{em}} = 2.95$. Our spectrum shows $\text{Mg II } \lambda\lambda 2796, 2803$ and $\text{C III] } \lambda 1909$, revealing that the true redshift is $z_{\text{em}} = 0.7165$. This QSO is therefore not suitable for our DLA survey and we do not include it in our main sample. We present the spectrum of this QSO in the Appendix and in Figure A1

In addition to the quasars listed in Table 2, we also attempted to obtain spectra of TXS1713+218 ($z_{\text{em}} = 4.01$, $B=22.0$) and TXS1835–345 ($z_{\text{em}} = 2.78$, $B=21.5$), both of which were observed at the VLT in service mode. Our spectrum of TXS1713+218 has very little flux bluewards of Lyman- α emission, so these data are not suitable for a DLA search. The spectrum of TXS1835–345 is clearly that of a late-type star and inspection of the acquisition images confirms that the wrong object was observed. We therefore exclude these two targets from our tables and figures.

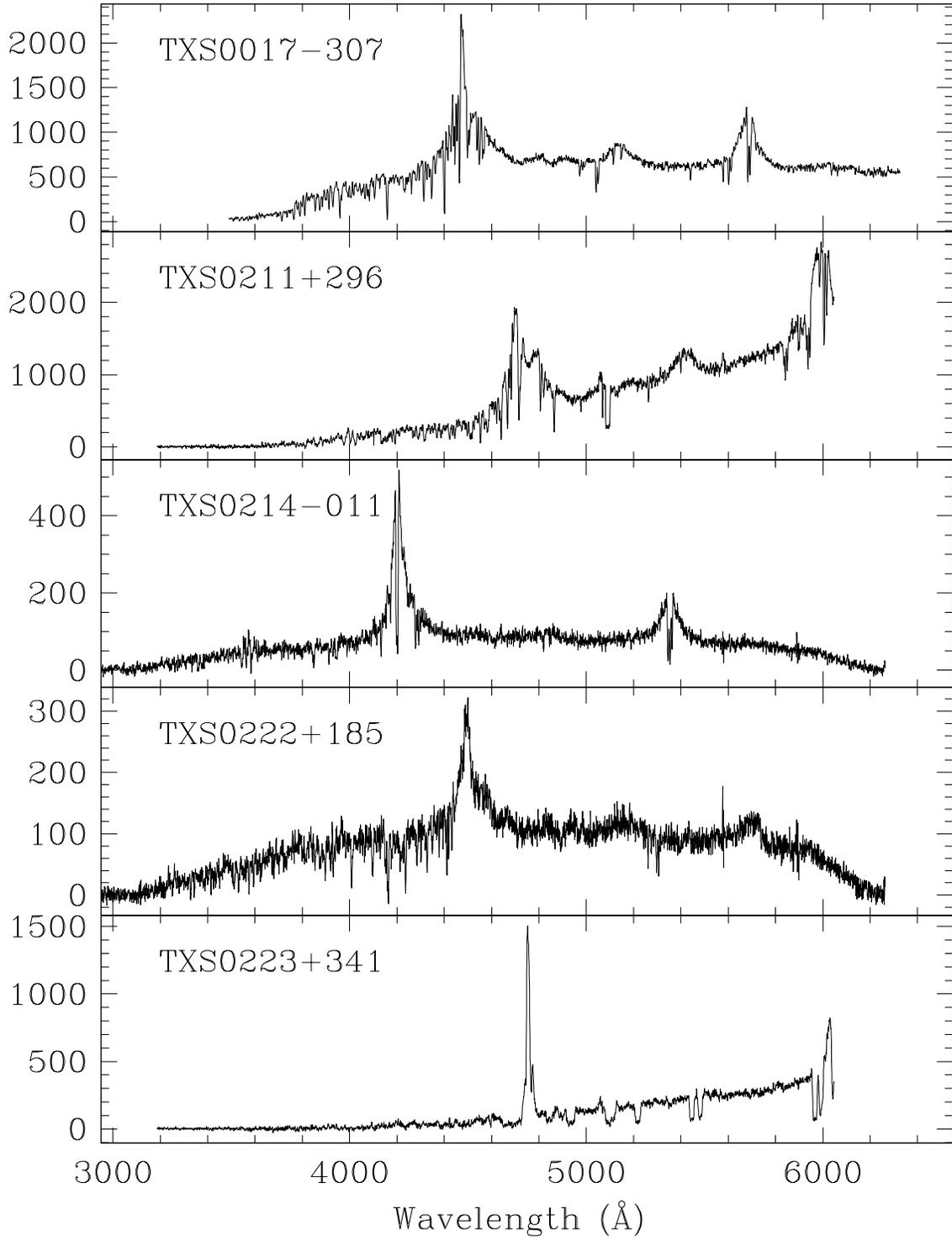


Figure 1. Spectra of the QSOs observed in our survey.

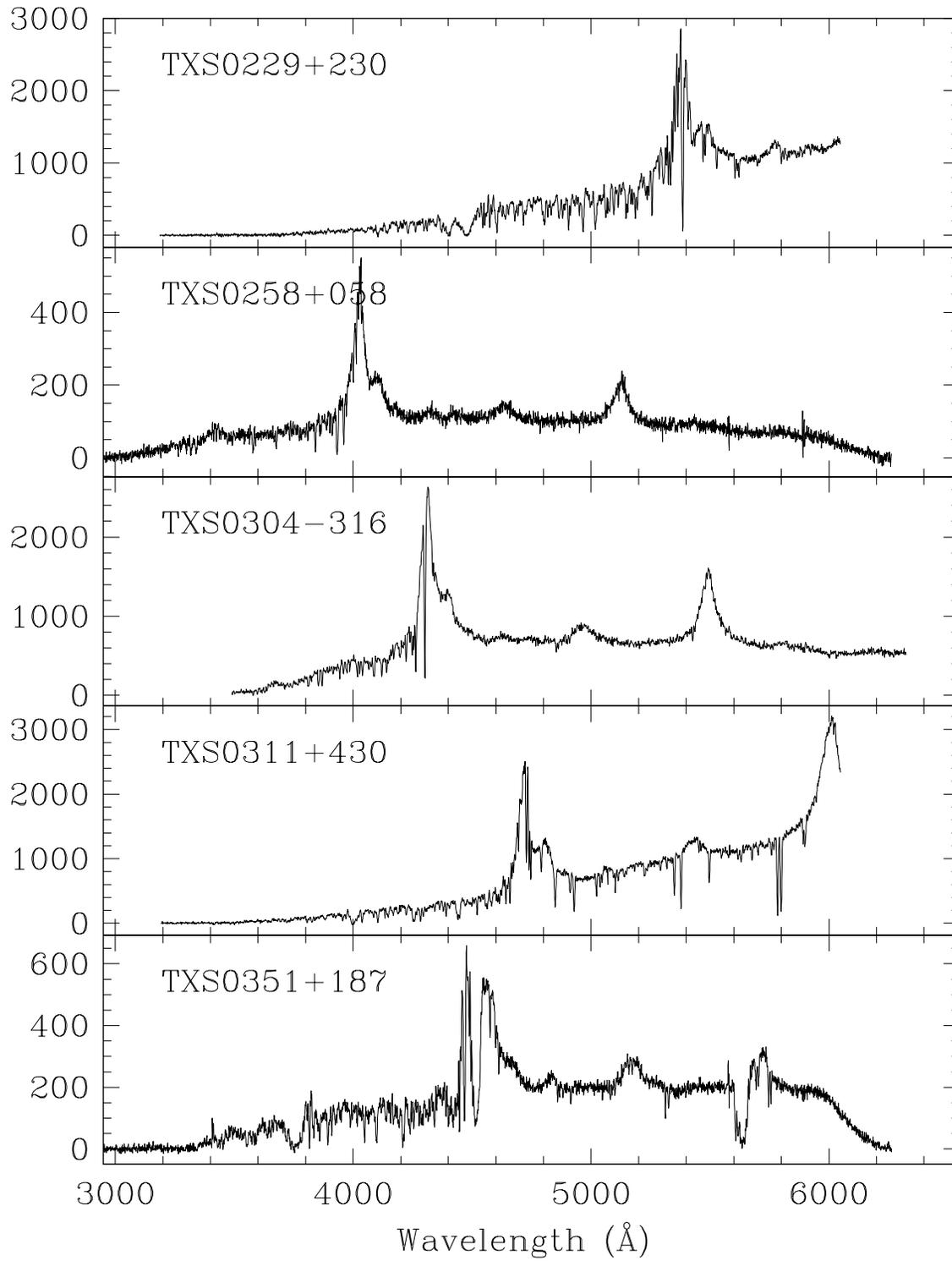


Figure 1. Continued.

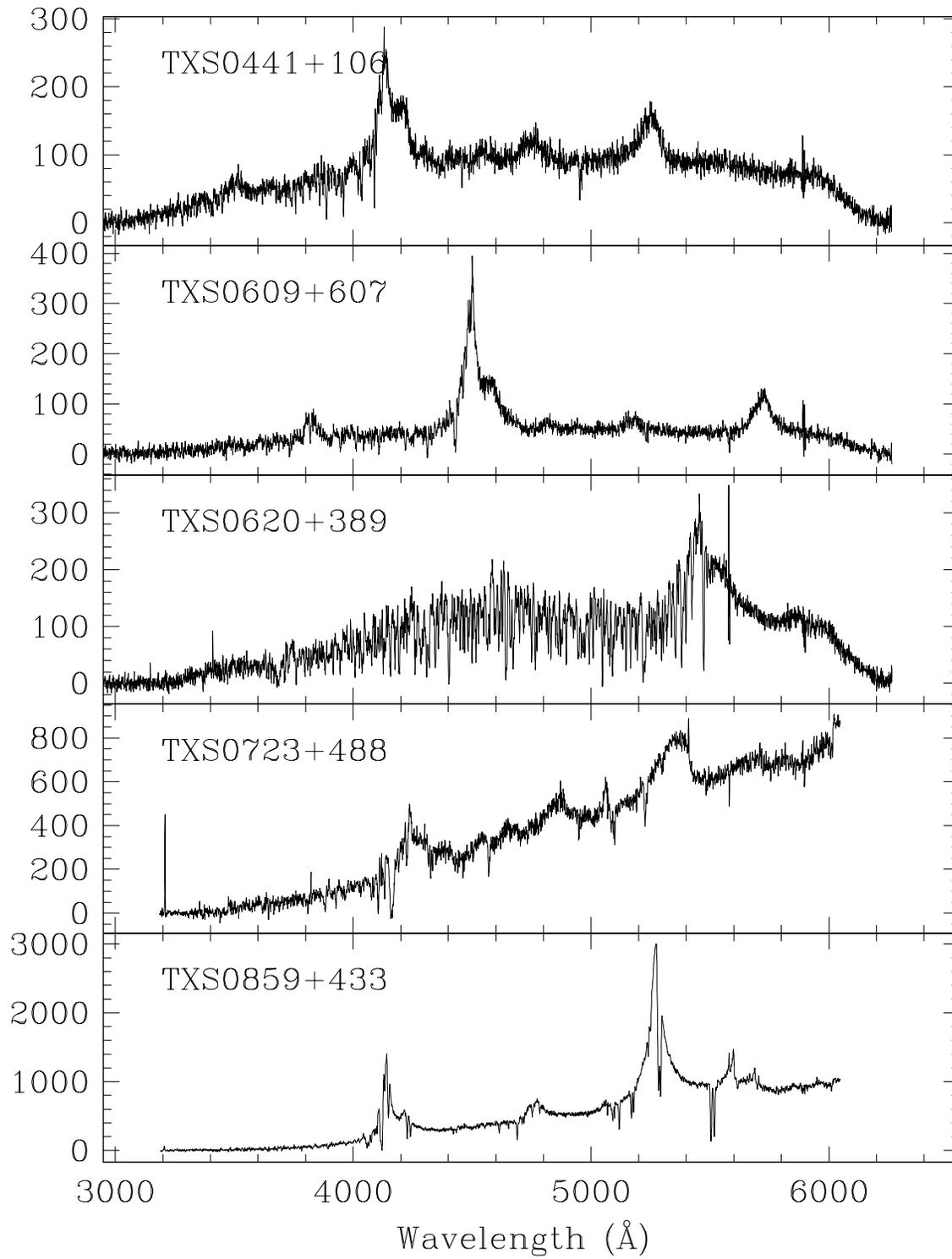


Figure 1. Continued.

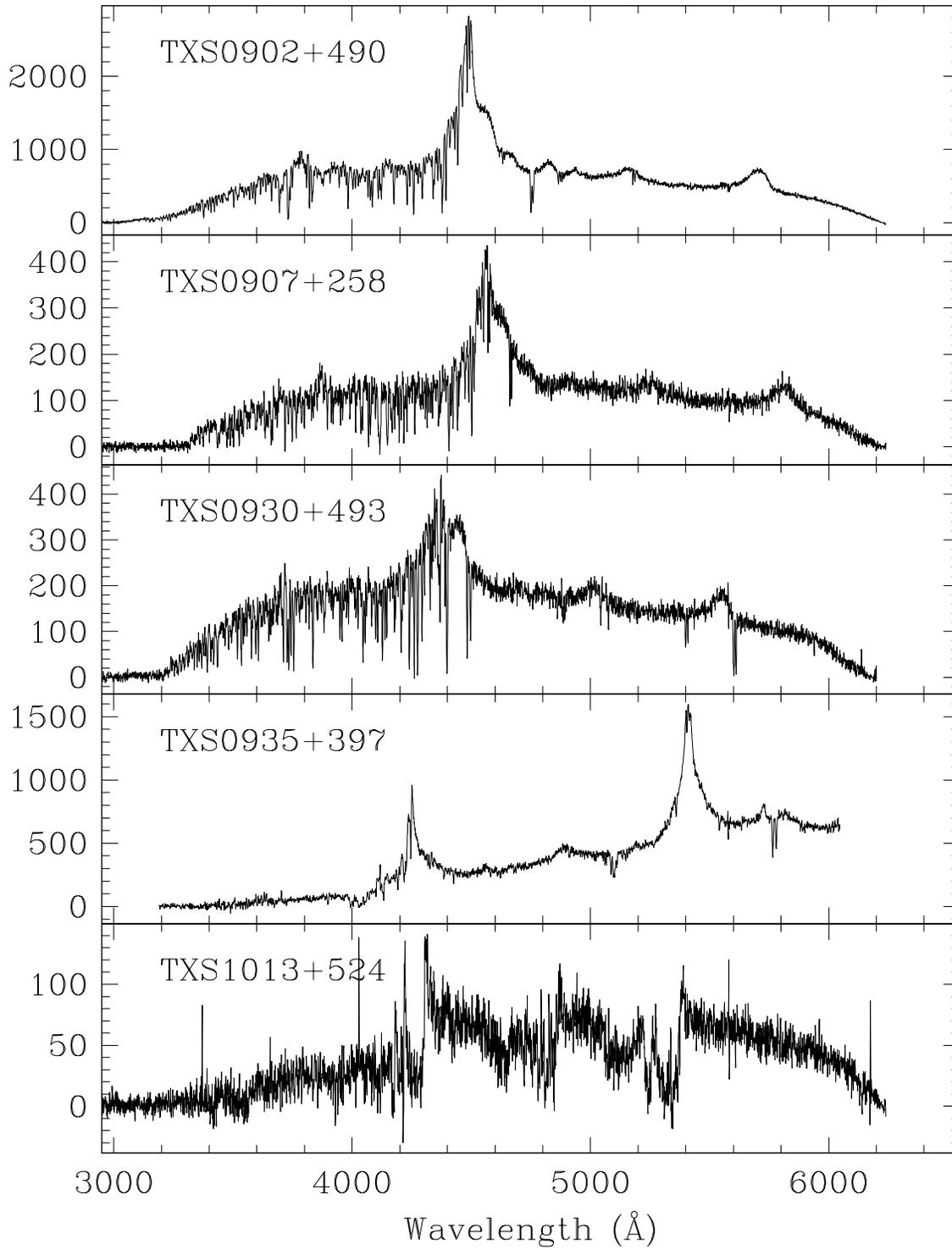


Figure 1. Continued.

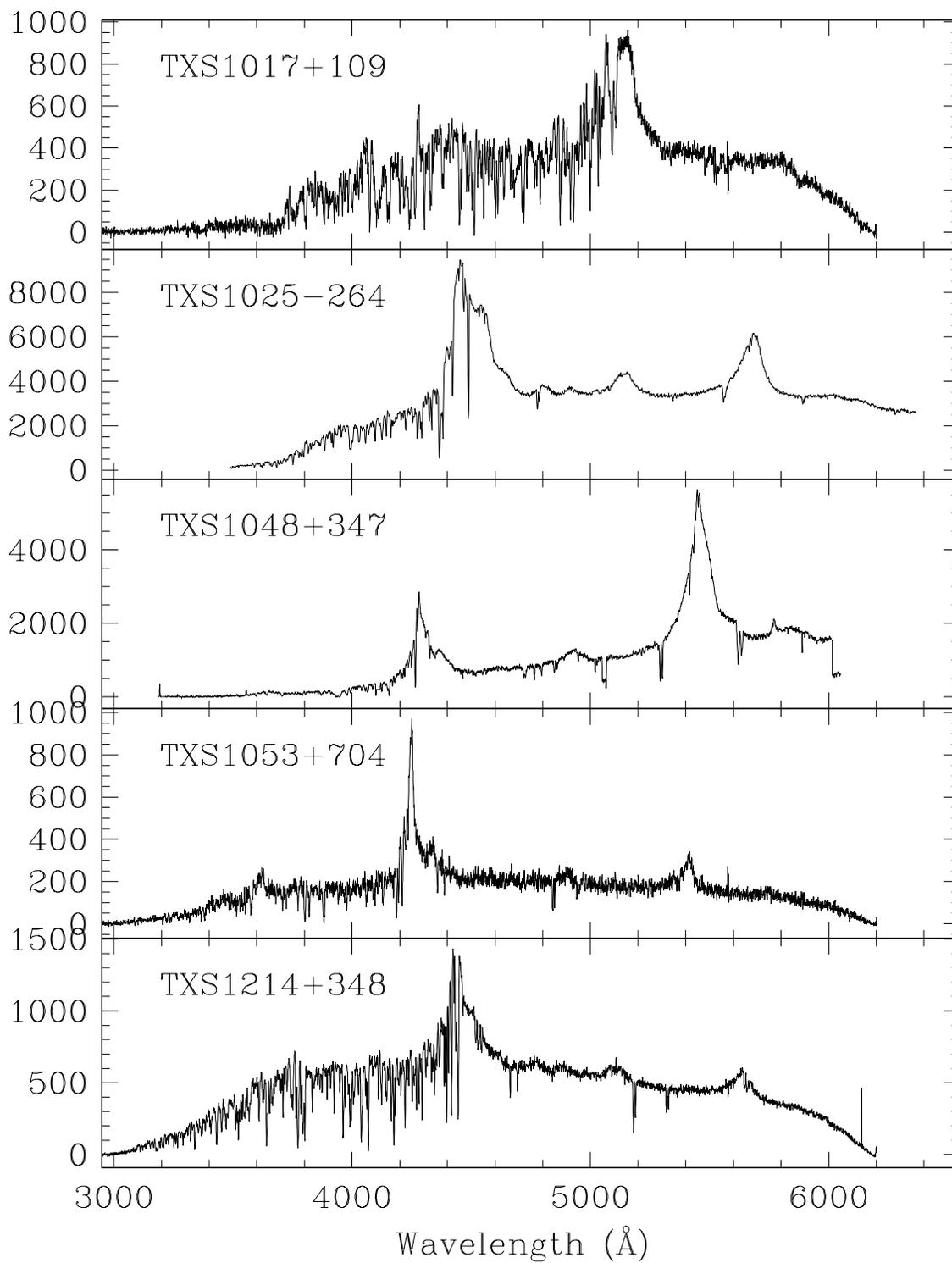


Figure 1. Continued.

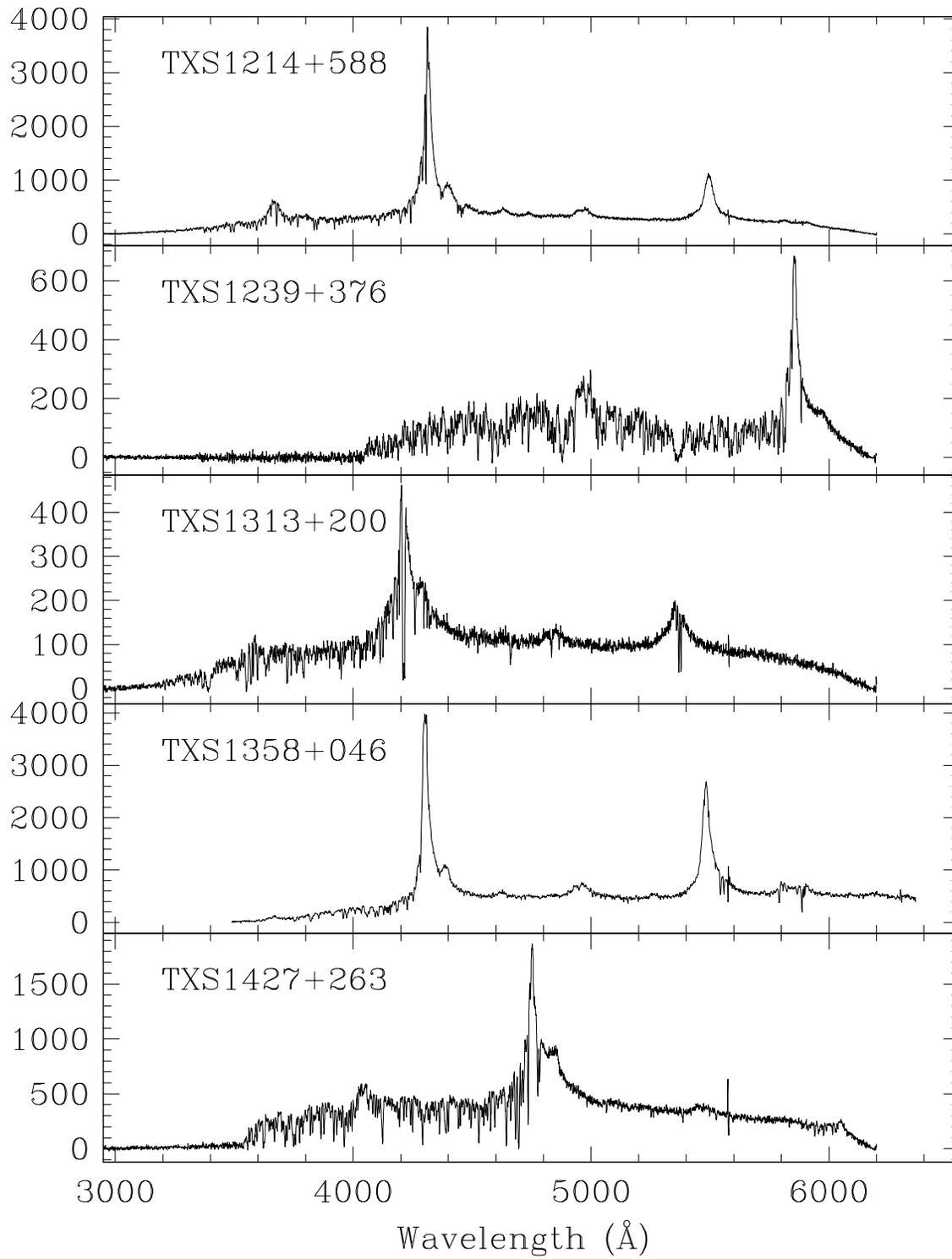


Figure 1. Continued.

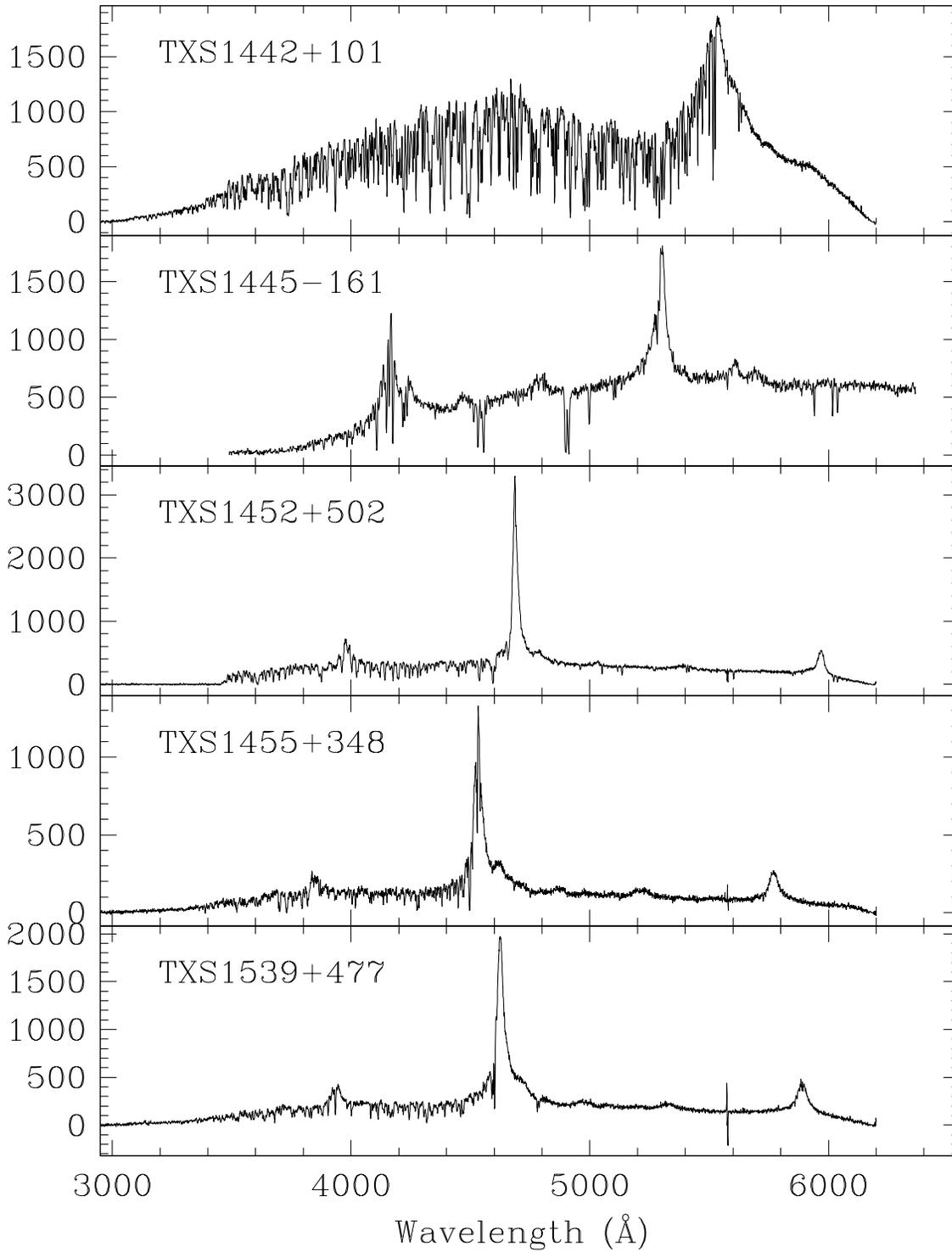


Figure 1. Continued.

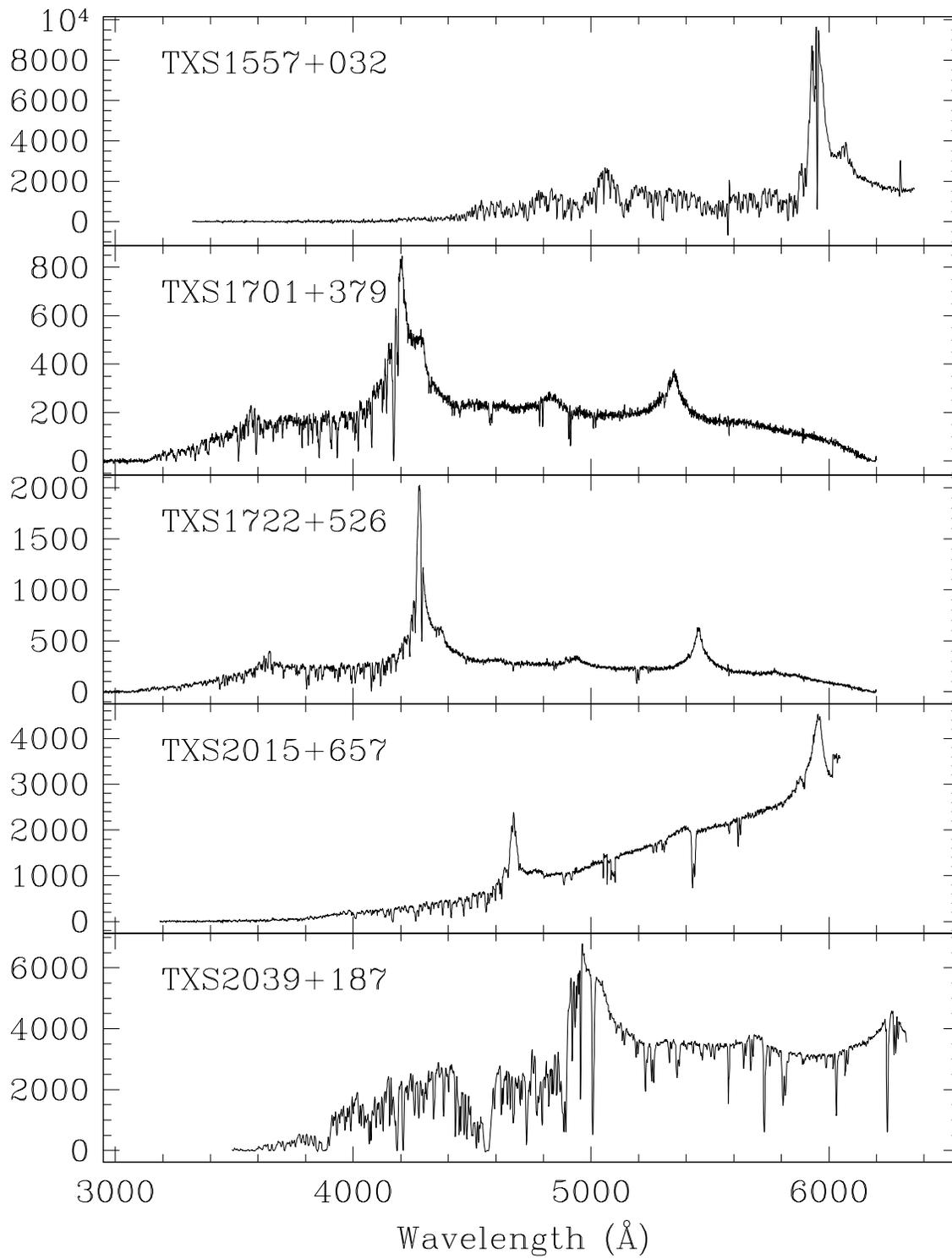


Figure 1. Continued.

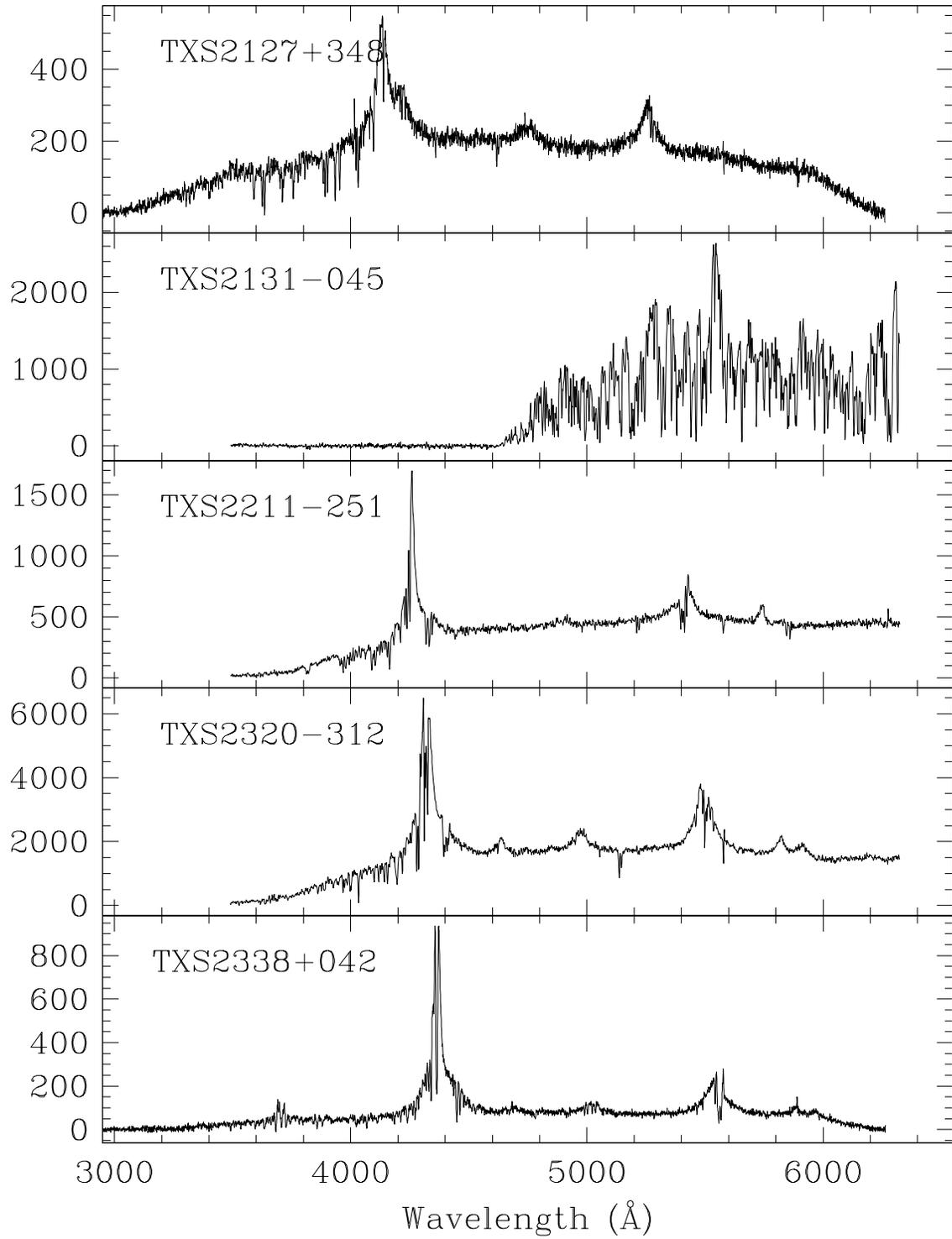


Figure 1. Continued.

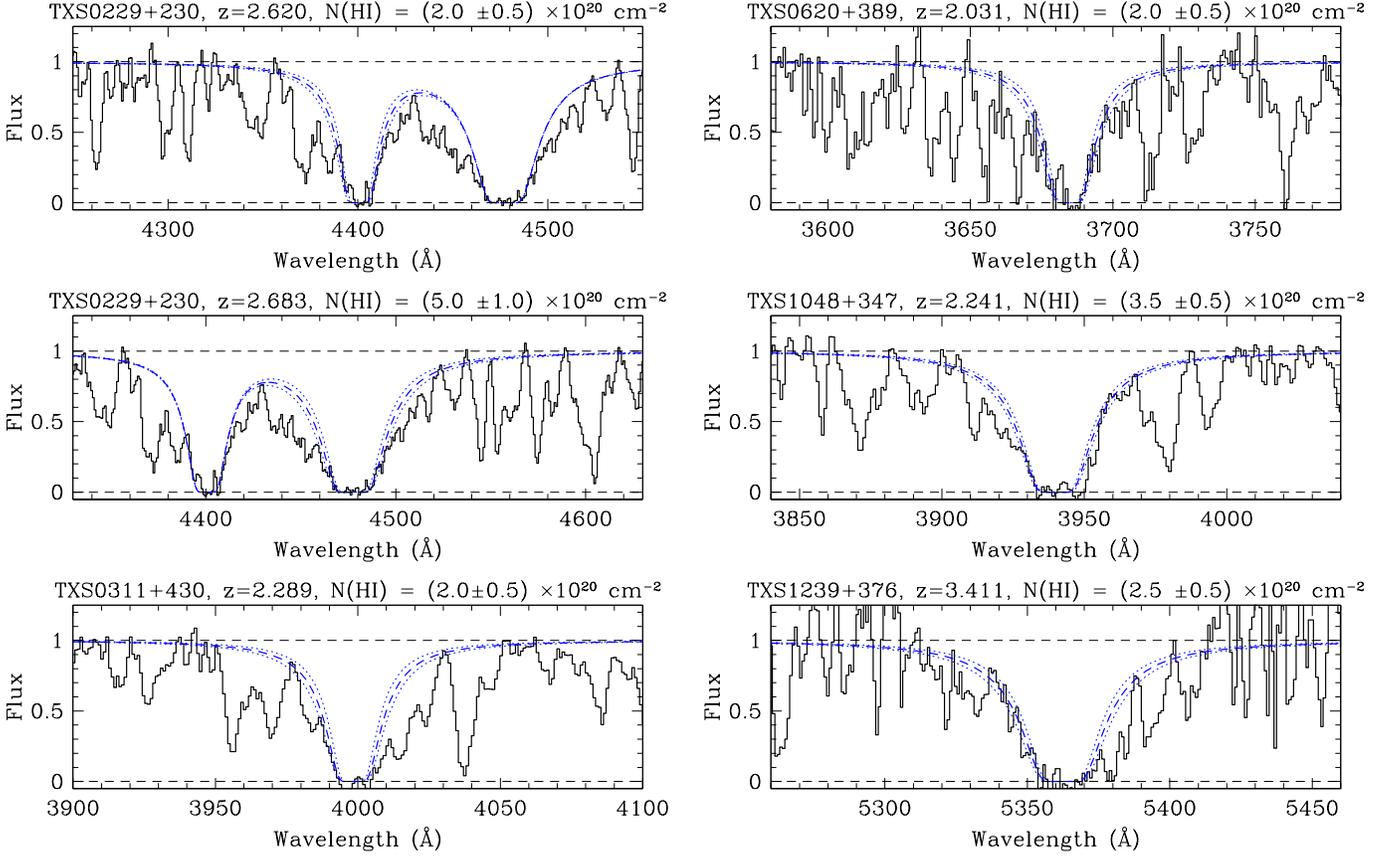


Figure 2. Profile fits to detected DLAs. There are two DLAs towards TXS0229+230, so the fit for each accounts for the damping wings of the other.

5 RESULTS

5.1 DLA detection

The spectra were visually inspected for DLA candidates. We searched for absorbers that were separated from the emission redshift of the QSO by at least 3000 km s^{-1} . This velocity cut-off (sometimes extended to 5000 km s^{-1}) has been a standard custom in DLA searches, largely to exclude absorption that may be associated with the QSO itself. However, further motivation for a velocity cut-off has been provided by Ellison et al. (2002) who found an excess of absorbers within 3000 km s^{-1} of a radio-loud QSO sample. Similar excesses have now also been confirmed towards radio-quiet QSOs (Russell, Ellison & Benn 2006; Prochaska, Hennawi & Herbert-Fort 2008), indicating that these ‘proximate’ absorbers may be galaxies clustered around the quasar³. The maximum redshift at which we search for DLAs is therefore

$$z_{\max} = \left[(z_{\text{em}} + 1) \sqrt{\frac{1-b}{1+b}} \right] - 1, \quad (1)$$

where

$$b = \frac{v}{c} = 0.01. \quad (2)$$

³ In any case, no proximate DLAs are present in our survey.

Figure 2. Continued. The residual flux in the Lyman- α trough of TXS0620+389 is almost certainly spurious, since it appears in only one of the two exposures. It may be caused, at least in part, by a cosmic ray event very close to the spectrum on the CCD that was not fully removed.

The minimum redshift at which a DLA can be identified is usually set by the blue wavelength coverage of the spectrum (see Table 3). However, in cases where a Lyman limit system (LLS) is present in the QSO spectrum within the redshift search range,

$$z_{\min} = \frac{(z_{\text{LLS}} + 1) \times 912}{1216} - 1. \quad (3)$$

The total redshift path for the survey is then

$$\Delta z = \sum_{i=1}^n (z_{i,\max} - z_{i,\min}). \quad (4)$$

For our survey of DLAs towards TXS sources, we cover a total redshift path of $\Delta z = 38.79$. The redshift path towards each individual quasar is given in Table 4.

DLA candidates were identified by their large rest frame equivalent widths (always in excess of 5 \AA), saturated absorption troughs and extended damping wings. Once identified, the candidate was confirmed by fitting the continuum around the absorber, normalizing the spectrum and comparing the absorption troughs with theoretical damped profiles. We identified a total of nine DLAs with $N(\text{HI}) \geq 2 \times 10^{20} \text{ cm}^{-2}$, plus one absorber with $N(\text{HI}) = 1.0 \times 10^{20} \text{ cm}^{-2}$. This latter system is technically a sub-DLA and we there-

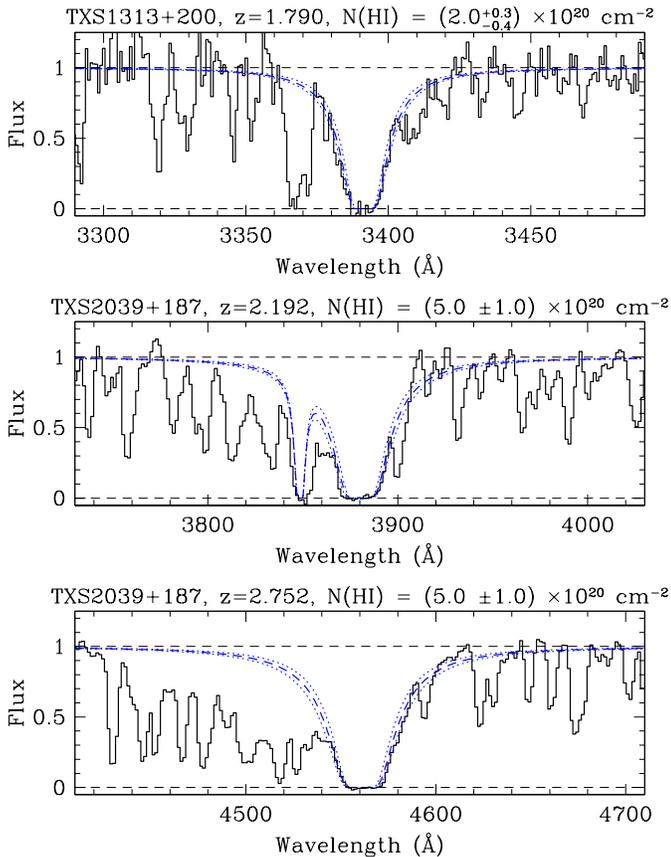


Figure 2. Continued. The Ly β transition of the $z_{\text{abs}} = 2.752$ DLA towards TXS2039+187 is accounted for in the fit of the $z_{\text{abs}} = 2.192$ DLA.

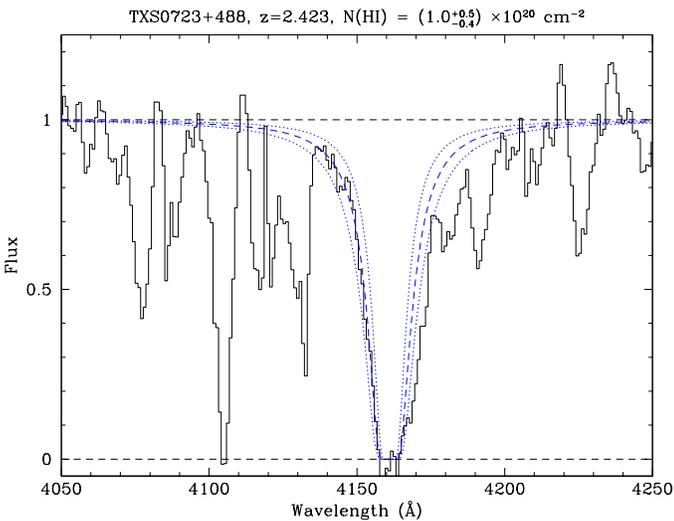


Figure 3. Profile fit to the detected sub-DLA.

fore exclude it from statements that refer specifically to DLA statistics. The Lyman- α line of the 10 absorbers and theoretical damped profiles are shown in Figures 2 and 3. One of the DLAs in our sample, towards TXS1239+376, has also been identified in the survey of Jorgenson et al. (2006), although this was not known at the time of our observations in April 2005. Jorgenson et al. (2006) determine a column density of $\log N(\text{H I}) = 20.30 \pm 0.15$; this value is slightly lower than our value of $\log N(\text{H I}) = 20.40^{+0.08}_{-0.10}$, although consistent within the errors. The QSO TXS0620+389 was also included in the Jorgenson et al. survey, yet these authors do not report the detection of a DLA in this sightline. The reason for this omission is that the rest-frame equivalent width measured for this absorber in the UCSD survey was $< 5 \text{ \AA}$, and it therefore did not pass the threshold to be considered as a candidate DLA (R. Jorgenson, private communication).

From the sample of nine DLAs, we derive a number density $n(z) = \#DLA/\Delta z = 0.23^{+0.11}_{-0.07}$, where the error bars are derived from the 1σ confidence limits applicable to small numbers, as tabulated by Gehrels (1986). The mean absorption redshift of our nine DLAs is $\langle z \rangle = 2.44$, a value that decreases slightly to $\langle z \rangle = 2.40$ if the single $z_{\text{abs}} < 2$ and $z_{\text{abs}} > 3$ DLAs are excluded. Our derived number density is therefore in good agreement with the functional fit to the SDSS-DR3 DLA sample (Prochaska, Herbert-Fort & Wolfe 2005): Eqn. 5 in Prochaska, Hennawi & Herbert-Fort (2008) yields $n(z) = 0.19$ for $\langle z \rangle = 2.44$. For comparison, the CORALS survey covered $\Delta z = 57.16$ and detected 19 DLAs at a mean absorption redshift of $\langle z \rangle = 2.50$ (Ellison et al. 2001). The UCSD survey covered $\Delta z = 41.15$ and detected 7 DLAs at a mean absorption redshift of $\langle z \rangle = 2.53$ (Jorgenson et al. 2006). The combined statistics of these two surveys yields $n(z) = 0.26^{+0.06}_{-0.05}$ (Jorgenson et al. 2006), indicating that the number density can be fairly robustly determined, even from relatively small samples. Unlike the CORALS and UCSD survey, our sample is not optically complete. The consistency of our number density with the both the SDSS-DR3 sample and the radio-selected CORALS and UCSD samples is further evidence that dust depletion is unlikely to significantly affect the derivation of $n(z)$ from magnitude-limited, optically-selected QSO samples (Ellison et al. 2001; Jorgenson et al. 2006).

5.2 Metals

For all of the DLAs detected in our survey, we checked the spectra for the presence of strong metal lines. Although most metal lines that can be detected at the S/N and resolution of our spectra are likely to be saturated, they are useful for constraining the absorption redshift of the DLA. In some cases, they may also be used to obtain a crude metallicity estimate. Our spectroscopic observations were designed to maximise coverage of the Lyman- α forest. Since many of the strong metal lines that are usually associated with DLAs are not within our spectral coverage, we restricted our search to the following species: Fe II λ 1608, Si II λ 1304, Si II λ 1526, Si II λ 1808, Al II λ 1670. In Table 5 we give measured rest frame equivalent widths and 3σ limits in the case of non-detections. The detection limits were calculated on the

Table 4. Absorber search statistics

QSO	z_{\max}	z_{\min}	Δz	z_{abs}	$N(\text{H I})$ (10^{20} cm^{-2})
TXS0017–307	2.63	1.90	0.73
TXS0211+296	2.83	2.04	0.79
TXS0214–011	2.42	1.63	0.79
TXS0222+185	2.65	1.63	1.02
TXS0223+341	2.87	2.45	0.42
TXS0229+230	3.38	2.06	1.32	2.620 ± 0.001 2.683 ± 0.002	2.0 ± 0.5 5.0 ± 1.0
TXS0258+058	2.28	1.59	0.69
TXS0304–316	2.50	1.90	0.60
TXS0311+430	2.83	2.04	0.79	2.289 ± 0.002	2.0 ± 0.5
TXS0351+187	2.67	1.75	0.92
TXS0441+106	2.37	1.63	0.74
TXS0609+607	2.66	1.80	0.86
TXS0620+389	3.42	1.71	1.71	2.031 ± 0.002	2.0 ± 0.5
TXS0723+488	2.43	1.96	0.47	2.423 ± 0.002	$1.0^{+0.5}_{-0.4}$
TXS0859+433	2.38	2.04	0.34
TXS0902+490	2.65	1.63	1.02
TXS0907+258	2.70	1.75	0.95
TXS0930+493	2.54	1.67	0.87
TXS0935+397	2.46	2.04	0.42
TXS1013+524	2.42	1.96	0.46
TXS1017+109	3.11	2.06	1.05
TXS1025–264	2.62	1.90	0.72
TXS1048+347	2.48	1.96	0.52	2.241 ± 0.002	3.5 ± 0.5
TXS1053+704	2.46	1.63	0.83
TXS1214+348	2.60	1.59	1.01
TXS1214+588	2.50	1.59	0.91
TXS1239+376	3.76	2.37	1.39	3.411 ± 0.003	2.5 ± 0.5
TXS1313+200	2.44	1.63	0.81	1.790 ± 0.002	$2.0^{+0.3}_{-0.4}$
TXS1358+046	2.51	1.90	0.61
TXS1427+263	2.87	1.96	0.91
TXS1442+101	3.48	1.63	1.85
TXS1445–161	2.38	2.00	0.38
TXS1452+502	2.80	1.88	0.92
TXS1455+348	2.69	1.63	1.06
TXS1539+477	2.76	1.59	1.17
TXS1557+032	3.84	2.50	1.34
TXS1701+379	2.42	1.63	0.79
TXS1722+526	2.48	1.59	0.89
TXS2015+657	2.80	2.04	0.76
TXS2039+187	3.01	2.00	1.01	2.192 ± 0.002 2.752 ± 0.001	5.0 ± 1.0 5.0 ± 1.0
TXS2127+348	2.37	1.59	0.78
TXS2131–045	4.18	2.91	1.27
TXS2211–251	2.47	1.92	0.55
TXS2320–312	2.50	1.90	0.60
TXS2338+042	2.55	1.80	0.75

assumption of a single unresolved component whose FWHM matches the instrumental resolution (FWHM_i). In the rest frame of the absorber this 3σ equivalent width (EW) limit corresponds to

$$EW(3\sigma) = \frac{3 \times \text{FWHM}_i}{S/N \times (1 + z_{\text{abs}})} \quad (5)$$

Equivalent widths were determined by fitting one or multiple gaussians, as well as direct integration across the entire absorption line. This process is repeated for various estimates of the continuum level. The quoted errors therefore reflect both the range of EWs that we measure from

the two methods, and an estimate of the continuum error. We compared the profiles of each metal line detection in velocity space in order to assess the potential contamination of metal lines by other species. If the contaminating component is at least partially resolved from the metal line of interest, we attempt to de-blend the components. However, if the contamination is severe, we do not report an EW and the entry ‘blended’ appears in Table 5. If the metal line is in the Lyman- α forest, the entry ‘Ly α ’ is given.

Although high resolution (typically, echelle) spectra are normally required to accurately measure DLA abundances, lower resolution spectra have been used to determine metal-

licities from weak absorption lines such as those of Zn II and Cr II (e.g. Pettini et al. 1997). However, high S/N ratios are required to detect such weak lines, and our spectra typically have detection limits that are too shallow for accurate metallicities to be derived. Nonetheless, we attempt a crude estimate of the metallicities of our survey DLAs. If any of the Si II or Fe II lines have EWs ≤ 0.20 Å we use the assumption of a linear curve of growth to determine the Si II or Fe II column density. In practice, this is likely to be a lower limit to the elemental column density if the line is partially saturated. Alternatively, we use the EW of the Si II $\lambda 1526$ Å transition as a rough metallicity indicator, following the correlation of Prochaska et al. (2008):

$$[M/H] = (-0.92 \pm 0.05) + (1.41 \pm 0.10) \log \text{EW}(\text{Si II } \lambda 1526) \quad (6)$$

Although the *mean* value of metallicity for a given EW (Si II $\lambda 1526$) is well determined from this calibration, often to better than 0.1 dex according to Prochaska et al. (2008), there is nevertheless a large spread in the metallicities of DLAs about the relation in Eqn 6. The metallicities of individual DLAs derived from this technique should therefore be treated with caution, and as rough estimates only.

The metallicity estimates and the technique from which they are derived are given in Table 6. In a number of cases, the metallicity can be derived from both Si II and Fe II lines. In all such cases $[\text{Si}/\text{H}] > [\text{Fe}/\text{H}]^4$, as is usually the case in DLAs due to preferential dust depletion of iron, and/or an enhancement of alpha-capture elements such as silicon. The metallicities that we obtain are mostly in the range of 1/30 to 1/100 of the solar value, typical of other DLAs at these redshifts (e.g. Prochaska et al. 2003). The three exceptions are the DLAs towards TXS0311+430, TXS1313+200 and the $z_{\text{abs}} = 2.752$ absorber towards TXS2039+187. Taking into account the two estimates of $[\text{Si}/\text{H}]$ in the DLA towards TXS0311+430, and acknowledging that the curve of growth value may actually be a lower limit, this DLA appears to have a metallicity of at least 1/16, and possibly as high as 1/4, of the solar value⁵. This DLA has also been found to be the only known case to date of a high redshift DLA with low spin temperature, $T_s = (138 \pm 36)$ K (York et al. 2007), supporting the anti-correlation between metallicity and spin temperature tentatively detected in earlier DLA samples (Kanekar & Chengalur 2001; Kanekar & Briggs 2004). If this is indeed the case, then the DLA towards TXS1313+200 and the $z_{\text{abs}} = 2.752$ absorber towards TXS2039+187 whose metallicities appear to be 1/3 – 1/10 and 1/3 of the solar value respectively, may also have low spin temperatures. It will therefore be interesting to confirm the unusually high metallicities of these DLAs with higher resolution spectroscopy. If they indeed arise in massive galaxies, as may be expected from the mass-metallicity relation observed in high redshift galaxies (Savaglio et al. 2005; Erb et al. 2006; Liu et al. 2008), Hubble Space Telescope images may be able to confirm their morphologies and luminosities.

⁴ $[\text{X}/\text{H}] = \log(N(\text{X})/N(\text{H I})) - \log(N(\text{X})/N(\text{H I}))_{\odot}$. Solar values from Lodders (2003).

⁵ Our Si II curve of growth abundance, $[\text{Si}/\text{H}] = -0.6$ is slightly lower than the value derived by York et al. (2007), who found $[\text{Si}/\text{H}] = -0.48$. This is due to a re-assessment of the continuum level.

Table 6. DLA metallicity estimates

QSO	z_{abs}	[M/H]	Method
TXS 0229+230	2.620	-1.6	Si II $\lambda 1526$ -[M/H] relation
TXS 0229+230	2.683	-2.2	Fe II $\lambda 1608$ linear COG
		-1.6	Si II $\lambda 1526$ -[M/H] relation
TXS 0311+430	2.289	-0.6	Si II $\lambda 1808$ linear COG
		-1.2	Si II $\lambda 1526$ -[M/H] relation
TXS 0620+389	2.031	...	N/A
TXS 0723+488	2.423	-1.4	Si II $\lambda 1304$ linear COG
		< -1.5	Fe II $\lambda 1608$ linear COG
TXS 1048+347	2.241	-1.7	Si II $\lambda 1526$ -[M/H] relation
		< -0.9	Si II $\lambda 1808$ linear COG
		-2.0	Fe II $\lambda 1608$ linear COG
TXS 1239+376	3.411	...	N/A
TXS 1313+200	1.790	< -0.4	Si II $\lambda 1808$ linear COG
		-1.0	Si II $\lambda 1526$ -[M/H] relation
TXS 2039+187	2.192	-1.4	Si II $\lambda 1808$ linear COG
		-2.1	Fe II $\lambda 1608$ linear COG
TXS 2039+187	2.752	-0.5	Si II $\lambda 1526$ -[M/H] relation

6 SUMMARY

We have presented the results of a survey for damped Lyman- α systems towards a sample of radio-selected QSOs. The sample was designed to identify DLAs that would be suitable for follow-up absorption spectroscopy in the redshifted H I 21 cm line. Our sample consists of 45 QSOs, covering a redshift path of $\Delta z = 38.79$, towards which we detect nine DLAs and one sub-DLA. The DLA number density is therefore $n(z) = 0.23_{-0.07}^{+0.11}$ at a mean absorption redshift of $\langle z \rangle = 2.44$, in good agreement with previous surveys of both optically- and radio-selected QSOs. We present fits to the damped profiles and derive H I column densities and measurements of metal line equivalent widths for all detected DLAs. We have already published an H I 21 cm detection towards one of these DLAs (TXS0311+430, $z_{\text{abs}} = 2.289$, $T_s = (138 \pm 36)$ K; York et al. 2007). In a future paper, Kanekar et al. (in preparation) will report the rest of the results of our follow-up H I 21 cm observations.

ACKNOWLEDGMENTS

SLE was funded by an NSERC Discovery grant. BAY was partially funded by an NSERC PGS-M award. NK acknowledges support from the Max-Planck foundation. The authors would like to thank the referee, Johan Fynbo, for his useful and prompt review of this work. This research has made use of the NASA/IPAC Extragalactic Database (NED) which is operated by the Jet Propulsion Laboratory, California Institute of Technology, under contract with the National Aeronautics and Space Administration. Based on observations obtained at the Gemini Observatory, which is operated by the Association of Universities for Research in Astronomy, Inc., under a cooperative agreement with the NSF on behalf of the Gemini partnership: the National Science

Table 5. Metal line equivalent widths and 3σ detection limits

QSO	z_{abs}	Fe II $\lambda 1608$ (Å)	Si II $\lambda 1304$ (Å)	Si II $\lambda 1526$ (Å)	Si II $\lambda 1808$ (Å)	Al II $\lambda 1670$ (Å)
TXS 0229+230	2.620	blended	Ly α	0.33 \pm 0.02
TXS 0229+230	2.683	0.13 \pm 0.02	Ly α	0.36 \pm 0.05
TXS 0311+430	2.289	0.21 \pm 0.02	Ly α	0.69 \pm 0.05	0.10 \pm 0.01	0.73 \pm 0.03
TXS 0620+389	2.031	Ly α	Ly α	Ly α	blended	Ly α
TXS 0723+488	2.423	<0.12	0.20 \pm 0.02	blended	...	0.15 \pm 0.02
TXS 1048+347	2.241	0.15 \pm 0.04	Ly α	0.26 \pm 0.06	<0.09	0.25 \pm 0.01
TXS 1239+376	3.411	...	Ly α
TXS 1313+200	1.790	0.23 \pm 0.05	Ly α	0.89 \pm 0.03	<0.18	0.97 \pm 0.05
TXS 2039+187	2.192	0.17 \pm 0.03	Ly α	Ly α	0.04 \pm 0.01	0.38 \pm 0.02
TXS 2039+187	2.752	1.12 \pm 0.03	Ly α	1.90 \pm 0.02	...	1.80 \pm 0.06

Foundation (United States), the Science and Technology Facilities Council (United Kingdom), the National Research Council (Canada), CONICYT (Chile), the Australian Research Council (Australia), Ministerio da Cincia e Tecnologia (Brazil) and SECYT (Argentina).

REFERENCES

- Braun, R., 1997, *ApJ*, 484, 637
Braun, R., & Walterbos, R. A. M., 1992, *ApJ* 386, 120
Briggs, F.H., Brinks, E., & Wolfe, A.M. 1997, *AJ*, 113, 467
Carilli, C. L., Lane, W., de Bruyn, A. G., Braun, R., Miley, G. K., 1996, *AJ*, 112, 1317
Chengalur, J. N., & Kanekar, N., 2000, *MNRAS*, 318, 303
Curran, S. J., Murphy, M. T., Pihlstrom, Y. M., Webb, J. K., Purcell, P. R., 2005, *MNRAS*, 356, 1509
Curran, S. J., Webb, J. K., 2006, *MNRAS*, 371, 356
de Bruyn, A.G., O’Dea, C.P., & Baum, S.A. 1996, *A&A*, 305, 450
Dodonov, S. N., Pariiskii, Y. N., Goss, W. M., Kopylov, A. I., Soboleva, N. S., Temirova, A. V., Verkhodlanov, O. V., Zhelenkova O.P., 1999, *ARep*, 43, 275
Douglas, J. N., Bash, F. N., Bozayan, F. A., Torrence, G. W.; Wolfe, C., 1996, *AJ*, 111, 1945
Ellison, S. L., Hennawi, J. F., Martin, C. L., Sommer-Larsen, J., 2007, *MNRAS*, 378, 801
Ellison, S. L., Yan, L., Hook, I., Pettini, M., Wall, J., Shaver, P., 2001, *A&A*, 379, 393
Ellison, S. L., Yan, L., Hook, I., Pettini, M., Wall, J., Shaver, P., 2002, *A&A*, 383, 91
Erb, D. K., Shapley, A. E., Pettini, M., Steidel, C. C., Reddy, N. A., Adelberger, K. L., 2006, *ApJ*, 644, 813
Ge, J., Bechtold, J., 1997, *ApJ*, 477, L73
Ge, J., Bechtold, J., Kulkarni, V., 2001, *ApJ*, 547, L1
Gehrels, N., 1986, *ApJ*, 303, 336
Haehnelt, M. G., Steinmetz, M., & Rauch, M. 1998, *ApJ*, 495, 647
Jorgenson, R., Wolfe, A. M., Prochaska, J. X., Lu, L., Howk, J. C., Cooke, J., Gawiser, E., Gelino, D., 2006, *ApJ*, 646, 730
Kanekar, N., Briggs, F. H., 2004, *NewAR*, 48, 1259
Kanekar, N., & Chengalur, J.N. 2001, *A&A*, 369, 42
Kanekar, N., & Chengalur, J.N. 2003, *A&A*, 399, 857
Kanekar, N., Chengalur, J. N., Lane, W. M., 2007, *MNRAS*, 375, 1528
Kanekar, N., Subrahmanyan, R., Ellison, S. L., Lane, W. M., Chengalur, J. N., 2006, *MNRAS*, 370, L46
Kulkarni, S. R., & Heiles, C., 1988, *Galactic and extragalactic radio astronomy* (2nd edition) Berlin and New York, Springer-Verlag, pages 95-153.
Lane, W., Smette, A., Briggs, F., Rao, S., Turnshek, D., Meylan, G. 1998, *AJ*, 116, 26
Ledoux, C., Petitjean, P., Srianand, R., 2003, *MNRAS*, 346, 209
Liszt, H. S., 2001, *A&A*, 371, 698
Liu, X., Shapley, A. E., Coil, A. L., Brinchmann, J., Ma, C.-P., 2008, *ApJ*, accepted
Lodders, K., 2003, *ApJ*, 591, 1220
Lopez, S., Reimers, D., D’Odorico, S., Prochaska, J. X., 2002, *A&A*, 385, 778
Lopez, S., Reimers, D., Gregg, M. D., Wisotzki, L., Wucknitz, O., Guzman, A., 2005, *ApJ*, 626, 767
Maller, A. H., Prochaska, J. X., Somerville, R. S., Primack, J. R., 2001, *MNRAS*, 326, 1475
Møller, P., Fynbo, J. P. U., & Fall, S. M., 2004, *A&A*, 422, L33
Noterdaeme, P., Ledoux, C., Petitjean, P., Le Petit, F., Srianand, R., Smette, A., 2007a, *A&A*, 474, 393
Noterdaeme, P., Petitjean, P., Srianand, R., Ledoux, C., Le Petit, F., 2007b, *A&A*, 469, 425
Noterdaeme, P., Ledoux, C., Petitjean, P., Srianand, R., 2008, *A&A*, 481, 327
Pettini, M., Smith, L.J., King, D.L., & Hunstead, R.W. 1997, *ApJ*, 486, 665
Prochaska, J. X., & Wolfe, A. M. 1997, *ApJ*, 487, 73
Prochaska, J. X., Howk, J. C., O’Meara, J. M., Tytler, D., Wolfe, A. M., Kirkman, D., Lubin, D., Suzuki, N., 2002, *ApJ*, 571, 693
Prochaska, J. X., Gawiser, E., Wolfe, A. M., Castro, S., Djorgovski, S. G., 2003, *ApJ*, 595, L9
Prochaska, J. X., Herbert-Fort, S., & Wolfe, A. M., 2005, *ApJ*, 635, 123
Prochaska, J. X., Chen, H.-W., Wolfe, A. M., Dessauges-Zavadsky, M., Bloom, J. S., 2008, *ApJ*, 672, 59
Prochaska, J. X., Hennawi, J. F., & Herbert-Fort, S., 2008, *ApJ*, 675, 1002
Russell, D., Ellison, S. L., Benn, C. R., 2006, *MNRAS*, 367, 412
Savaglio, S., et al., 2005, *ApJ*, 635, 260
Srianand, R., Petitjean, P., Ledoux, C., Ferland, G., Shaw, G., 2005, *MNRAS*, 362, 549

Tripp, T. M., Jenkins, E. B., Bowen, D. V., Prochaska, J. X., Aracil, B., Ganguly, R., 2005, ApJ, 619, 714
Tumlinson, J., et al., 2002, ApJ, 566, 857
Wolfe, A. M., & Davis, M. M., 1979, AJ, 84, 699
Wolfe, A. M., Briggs, F. H., Jauncey, D. L., 1981, ApJ, 248, 460
Wolfe, A. M., Briggs, F. H., Turnshek, D. A., Davis, M. M., Smith, H. E., Cohen, R. D., 1985, ApJ, 294, L67
Wolfe, A.M., Prochaska, J.X., & Gawiser, E., 2003, ApJ, 593, 215
Wolfe, A. M., Prochaska, J. X., Jorgenson, R. A., Rafelski, M., 2008, ApJ, accepted
York, B. A., Kanekar, N., Ellison, S. L., Pettini, M., 2007, MNRAS, 382, 53
Young, L., Lo, K., 1997, ApJ, 490, 710

**APPENDIX A: UPDATED REDSHIFT FOR
TXS2034+046**

We have obtained a spectrum of TXS2034+046 which is reported in Dodonov et al. (1999) to have an emission redshift $z_{\text{em}} = 2.95$. Figure A1 shows the spectrum obtained at the WHT where emission lines corresponding to Mg II $\lambda\lambda 2796, 2803$ and C III] $\lambda 1909$ reveal that the true redshift is $z_{\text{em}}=0.7165$.

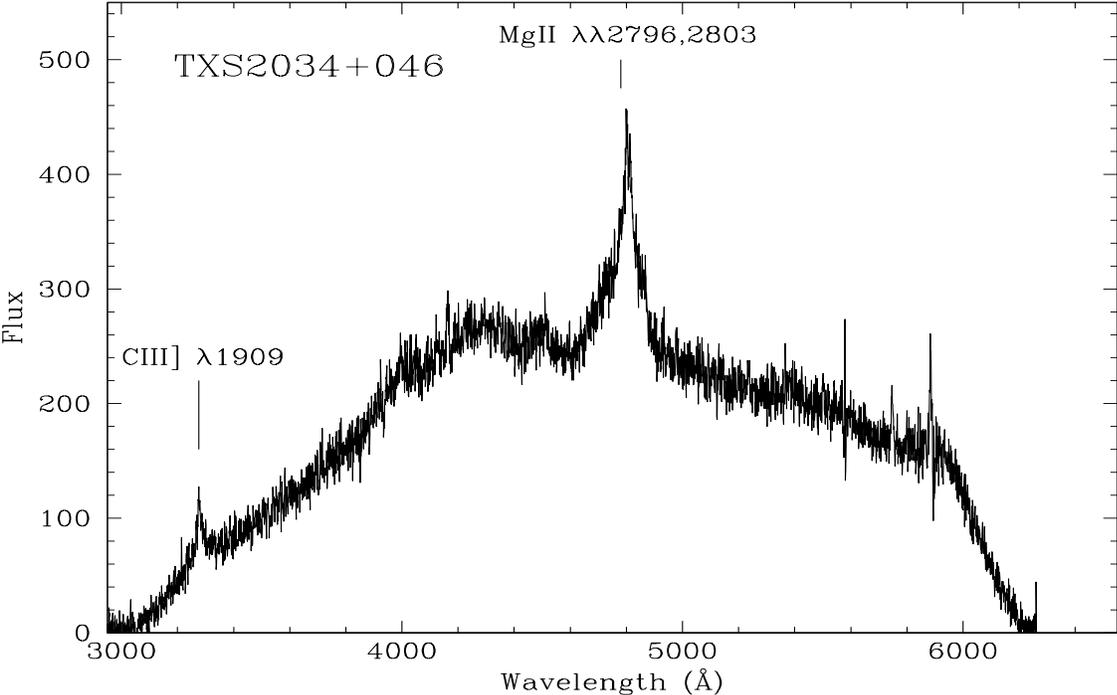


Figure A1. The spectrum of TXS2034+046, revealing its true redshift to be $z_{em}=0.7165$.